Ocean Modelling 24 (2008) 1–14

Contents lists available at ScienceDirect

Ocean Modelling

journal homepage: www.elsevier.com/locate/ocemod

Sea ice–ocean coupling using a rescaled vertical coordinate z^*

Jean-Michel Campin *, John Marshall, David Ferreira

Department of Earth, Atmospheric and Planetary Sciences, Massachusetts Institute of Technology, Cambridge, MA 02139, USA

ARTICLE INFO

Article history:
Received 24 September 2007
Received in revised form 4 April 2008
Accepted 1 May 2008
Available online 21 May 2008

Keywords:
Ocean model
Sea ice model
Free-surface
Vertical coordinate

ABSTRACT

Realistic representation of sea ice in ocean models involves the use of a non-linear free-surface, a real freshwater flux and observance of requisite conservation laws. We show here that these properties can be achieved in practice through use of a rescaled vertical coordinate "z^*" in z-coordinate models that allows one to follow undulations in the free-surface under sea ice loading. In particular, the adoption of "z^*" avoids the difficult issue of vanishing levels under thick ice.

Details of the implementation within MITgcm are provided. A high resolution global ocean sea ice simulation illustrates the robustness of the z^* formulation and reveals a source of oceanic variability associated with sea ice dynamics and ice-loading effects. The use of the z^* coordinate allows one to achieve perfect conservation of fresh water, heat and salt, as shown in extended integration of coupled ocean sea ice atmospheric model.

1. Introduction

The importance of conserving heat, fresh water and salt is crucial for ocean–sea ice models and coupled atmosphere sea ice–ocean GCMs (Schmidt et al., 2004), especially to prevent drift in long term simulations. This is particularly true in high-latitudes, where the exchange of water (solid or liquid) is relatively large and associated with significant heat content differences and with strong time variability (such as large seasonal cycles in Arctic river run-off). Indeed, the fidelity of coupled ocean sea ice simulations is sensitive to the manner in which the high-latitude fresh-water flux is treated in ocean models (Prange and Gerges, 2006).

Generally, each component of a coupled model strictly enforces conservation, based on a consistent set of approximations (e.g., volume instead of mass conservation in a Boussinesq ocean model). However, "leaks" (spurious sources and sinks) can appear when coupling different components each with their own different – albeit internally consistent – conservation rules. For example, the internal energy associated with precipitation (temperature, solid or liquid) is generally neglected in ocean models, but represents a crucial part of a sea ice model where snow is concerned (similarly for snow over land).

To avoid conservation problems related to the sea ice interface, Schmidt et al. (2004) made the following recommendations:

- to carefully define the interface between each component and fluxes across the interface;
- to account for the energy content (relative to an energy reference level, ERL) and tracer content of any mass exchange between the different components using a uniquely defined ERL across all components;

For example, and in particular, the height of the water column under sea ice needs to be allowed to vary when sea-water freezes (or sea ice melts), since the corresponding fresh water amount has to be taken out (or be added into) the uppermost ocean grid box (the so called "real fresh-water flux" formulation).

Despite advantages in term of realism and conservation, several z-coordinate ocean sea ice models do not allow mass exchange between ice and ocean (see Schmidt et al., 2004, their Sections 6 and 7, Johns et al., 2006). Historically, this was in part because of the need to employ a time-varying upper level thickness which follows sea-surface undulations (the so called "non-linear free-surface"). Almost all modern ocean GCM's presently employ a non-linear free-surface (Griffies et al., 2001; Roullet and Madec, 2000) and so this is not now a limitation. However, there is another, more challenging, problem. As pointed out by Schmidt et al. (2004), there are potential numerical problems which occur when the surface level becomes very thin or even vanishes, in regions of thick ice compared to the depth of the upper ocean grid cell. Some crude and unphysical remedies are sometime used to avoid this problem (e.g., Griffies et al., 2005). This difficulty is specific to z-coordinate models, since isopycnal or terrain following coordinate ocean sea ice models have already adopted a realistic mass exchange formulation,

* Corresponding author. Tel.: +1 617 253 0098; fax: +1 617 253 4464.
E-mail addresses: jmc@mit.edu (J.-M. Campin), jmarsh@mit.edu (J. Marshall), dfer@mit.edu (D. Ferreira).

1463-5003/$ - see front matter © 2008 Elsevier Ltd. All rights reserved.
doi:10.1016/j.ocemod.2008.05.005

even under the huge ice-loading effect of an ice-shelf (Holland and Jenkins, 2001; Timmermann et al., 2002).

Recently, Adcroft and Campin (2004) described the rescaled height coordinates (z^*) formulation as a solution to the problem of vanishing surface levels under large sea-surface displacement, whilst retaining the convenience of a height coordinate. Here we describe how the z^* coordinate approach can be used to solve the sea ice interface problem by allowing one to consider mass exchange between ice and ocean in an exact way, without any of the inconveniences of the traditional z-coordinate. A similar approach, but applied to a mass coordinate ocean model, is used in the GISS coupled climate model (Russell et al., 1995).

Our paper is set-out as follows: in Section 2 we formulate the problem in terms of z^*; Sections 3 and 4 illustrates the successful implementation of sea ice–ocean mass exchange with a z^* coordinate: a "realistic" global set-up at relatively high resolution ($\simeq 1/6°$, Section 3), that includes sea ice dynamics emphasizes the dynamical response; a GFD-type, idealized low resolution coupled configuration on an aqua-planet (Section 4) over climatic timescales serves to illustrate the all-important conservation properties of mass, salt and heat. Finally, we summarize and conclude in Section 5.

2. Formulation of the coupling between sea ice and ocean models in z^* coordinates

The ice–ocean mass exchange formulation discussed here is not, strictly speaking, "new" (as mentioned in Schmidt et al. (2004)), but for clarity, and to make the connection with z^*, it is useful to present: (1) the equations incorporating ice–ocean mass exchange which apply to all non-linear free-surface models, independently of vertical coordinate; (2) the simplified formulation without ice–ocean mass exchange, emphasizing drawbacks, in particular in the treatment of salt flux; (3) the implications for sea ice dynamics; (4) the z^* solution to the current z-coordinate implementation; and finally, (5) the time-stepping algorithm.

2.1. Ice–ocean mass exchange formulation

The column integrated mass, salt and heat budget of a Boussinesq fluid are expressed:

$$\frac{\partial h}{\partial t} = -\nabla\cdot\int_{-H}^{\eta}\mathbf{u}_w\mathrm{d}z + F_m/\rho_w \tag{1}$$

$$\frac{\partial h\bar{S}}{\partial t} = -\nabla\cdot\int_{-H}^{\eta}S\mathbf{u}_w\mathrm{d}z + F_S/\rho_w \tag{2}$$

$$\frac{\partial h\bar{\theta}}{\partial t} = -\nabla\cdot\int_{-H}^{\eta}\theta\mathbf{u}_w\mathrm{d}z + F_H/(c_w\rho_w) \tag{3}$$

$$\text{with}: \bar{S} = \frac{1}{h}\int_{-H}^{\eta}S\mathrm{d}z \quad \text{and} \quad \bar{\theta} = \frac{1}{h}\int_{-H}^{\eta}\theta\mathrm{d}z$$

where η is the position of the ocean surface (below the ice), h is the column thickness ($h = \eta + H$, with the ocean bottom at $z = -H < 0$), $\mathbf{u}_w$ the water horizontal velocity, θ and S the potential temperature and salinity, ρ_w and c_w the reference density and heat capacity of sea-water, F_m,F_S and F_H the mass, salt and heat fluxes in units of kg/m^2/s, psu kg/m^2/s ($\simeq$g/m^2/s) and W/m^2, respectively. Diffusion is not considered here, but could easily be added to the right-hand-side of Eqs. (2) and (3).

Further terms can be added to Eqs. (3) and (2), to account for the heat content and salt content of the water mass flux[1]: $+\theta_m\cdot F_m/\rho_w$ and $+S_m\cdot F_m/\rho_w$ where S_m and θ_m are, respectively, the salinity and temperature of the fresh-water flux (precipitation, evaporation, run-off). Without any loss of generality, here the heat content of the fresh-water flux is considered to be part of the heat flux F_H[2]; similarly for salinity, in the few cases where $S_m\cdot F_m$ is non-zero, it can be considered to be part of F_S, as, for instance, when salty sea ice melts or when the small amount of salt that some rivers bring to the ocean is accounted for. This approach is consistent with the "energy reference level" concept developed by Schmidt et al. (2004); it also simplifies Eqs. (2) and (3) and avoids the need to distinguish between the various temperatures of all the fresh-water flux components (evaporation, rain, snow, run-off, ice melting and freezing) as far as the ocean is considered. On the other hand, an accurate evaluation of those fresh-water related contributions is easy to derive from a coupled atmospheric component, sea ice model or bulk-formulae over open ocean, and convenient to combine with heat and salt fluxes.

At the sea ice–ocean interface, because sea-water freezing (ice melting) is a positive (negative) contribution to the mass budget of the sea ice component, the same mass flux needs to be subtracted from (added to) the ocean component: melting and freezing are part of the mass flux F_m into the ocean. This also implies that the ocean upper boundary (surface, position η) is the ice–ocean interface where ice is present, and the open ocean surface elsewhere.

The hydrostatic pressure P_{hyd} term in ocean horizontal momentum equation:

$$\partial\mathbf{u}_w/\partial t = -1/\rho_w\nabla P_{hyd} + [\text{Coriolis},\ \text{Advection}, \text{Viscosity}] \tag{4}$$

is computed from:

$$P_{hyd} = P_{z=\eta} + \int_z^{\eta}\rho g\mathrm{d}z \quad \text{with } P_{z=\eta} = P_{atm} + gM_{(ice+snow)} \tag{5}$$

and accounts for atmospheric pressure (P_{atm}) and the weight of sea ice and snow ($gM_{ice+snow}$). Although the ocean–ice interface moves up (down) with melting (freezing) the oceanic hydrostatic pressure is not affected by sea ice melting or freezing, as the amount of water in the column remains unchanged. And indeed, in the case where only melting/freezing is considered, $\partial M/\partial t = -F_m$ balances[3] $\partial\eta/\partial t = F_m/\rho_w$ and the hydrostatic pressure P_{hyd} in Eq. (5) will not change.

For clarity, it is useful to define the sea-level position that one would measure in drilling a hole through the ice: $\eta^{leads} = \eta + M_{ice+snow}/\rho_w$. In the limit where salinity differences between sea ice and sea-water can be neglected, η^{leads} corresponds approximately to the mean sea-level position "as if" all the ice had melted.

In a numerical model, according to the finite-volume discretization, the model sea-surface position $[\eta]$[4] of a partially ice-covered mesh (ice fraction: ϕ) is defined as the weighted average of the sea-surface position in the two fractions of the grid cell, under the ice ($\eta|_{ice}$) and in the open water ($\eta|_{water}$):

$$[\eta] = \phi\cdot\eta|_{ice} + (1-\phi)\cdot\eta|_{water}$$

[1] Those terms are viewed as part of fresh water advection across the interface by Jenkins et al. (2001).

[2] For example, when the "energy reference level" corresponds to liquid water at 0 °C, melting of fresh snow at 0 °C implies only latent heat exchange. In contrast, when basal melting occurs, the heat flux that the sea ice component returns to the ocean accounts for the freezing temperature of sea-water in addition to the latent heat.

[3] The cancellation is almost exact, apart from the small density difference between the surface and the Boussinesq reference ρ_w.

[4] The bracket notation "[]" is intended to distinguish the discretized variable that the model uses from the continuous one. However, this specific notation is dropped when the context is clear enough and no risk of ambiguity exists.

Since our definition of η^{leads} corresponds precisely to $\eta|_{\text{water}}$, this allows one to express the grid cell average sea-surface position $[\eta]$ as equal to:

$$[\eta] = \phi \cdot \eta|_{\text{ice}} + (1-\phi) \cdot \eta^{\text{leads}} = \eta^{\text{leads}} - [M]_{\text{ice+snow}}/\rho_{\text{w}}$$

with the grid cell average $[M]_{\text{ice+snow}} = \phi \cdot (\rho_{\text{ice}} H_{\text{ice}} + \rho_{\text{snow}} H_{\text{snow}})$.

Two types of difficulties can be encountered when attempting to use this simple and most realistic boundary condition at the surface (so called "real fresh-water" exchange):

Firstly, from a pure implementation point of view, it demands that one deals with a varying ocean column thickness (at least, the surface level thickness) in all the model equations, including the barotropic dynamics, resulting in a non-linear free-surface formulation. This implementation is not always available (Prange and Gerges, 2006) or is source of technical difficulties (e.g.: to derive the adjoint, P. Heimbach, personal communication).

Secondly, when sea-surface position is strongly depressed, and reaches the first vertical interface, the surface level vanishes. This situation can be relatively common under heavy sea ice-loading, with fine vertical resolution as is typically in use near the surface. This is illustrated in Fig. 1b by the left column and corresponds to a situation where the condition:

$$\Delta z_1 + [\eta] = \Delta z_1 + \eta^{\text{leads}} - [M]_{\text{ice+snow}}/\rho_{\text{w}} > 0 \tag{6}$$

is not satisfied, with Δz_1 corresponding to the vertical grid spacing at the uppermost level.

Most large-scale z-coordinate OGCM are not able to deal with disappearing levels, and so would require significant effort and special coding (see how isopycnal models deal with infinitely thin layer thickness, e.g.: (Bleck, 2002)). For these reasons, many z-coordinate ocean sea ice models still use a simplified formulation, as detailed below.

2.2. Simplified formulation: no mass exchange

A commonly used approximation is to ignore the surface mass flux and associated fresh-water flux and to retain only its dilution/concentration effect on ocean salinity. Regarding the sea-surface position in the presence of sea ice, since no mass is taken out of the ocean when sea ice forms, freezing/melting does not affect the sea-surface elevation. Additionally, for consistency, ice-loading should not be considered so that oceanic hydrostatic pressure is not affected by freezing/melting as in the real world. As a consequence, the sea-surface is not depressed under the ice (Fig. 1a), "as if" the ice had melted (sometimes ironically called "levitating" sea ice), $\tilde{\eta} \equiv \eta^{\text{leads}}$ and the disappearing of the surface level under thick sea ice is no longer an issue. Here, in this section, the notations $\tilde{\eta}$ and $\tilde{h}$ are used to differentiate the approximated sea-surface position and water column thickness from the unapproximated one, η and h, as defined in Section 2.1.

This approximation results in a different equation for the water column thickness $\tilde{h}$:

$$\frac{\partial \tilde{h}}{\partial t} = \frac{\partial h}{\partial t} - F_{\text{m}}/\rho_{\text{w}} = -\nabla \cdot \int_{-H}^{\eta} \mathbf{u}_{\text{w}} \mathrm{d}z$$

The evolution of salinity can be expressed as

$$\frac{\partial \tilde{h}\overline{S}}{\partial t} = \frac{\partial h\overline{S}}{\partial t} + S_{\text{s}} \frac{\partial(\tilde{h}-h)}{\partial t} + (\tilde{h}-h)\frac{\partial \overline{S}}{\partial t} \tag{7}$$

with S_{s} being the surface salinity. The first term is given by Eq. (2), and the second term is equal to $-S_{\text{s}} \cdot F_{\text{m}}/\rho_{\text{w}}$ and appears on the right-hand-side as a virtual salt flux. The approximate "virtual salt flux" formulation neglects the third and last term $(\tilde{h}-h)\partial\overline{S}/\partial t$ and similarly the equivalent term in the heat budget, so that the column mass, salt and heat budget Eqs. (1)–(3) become:

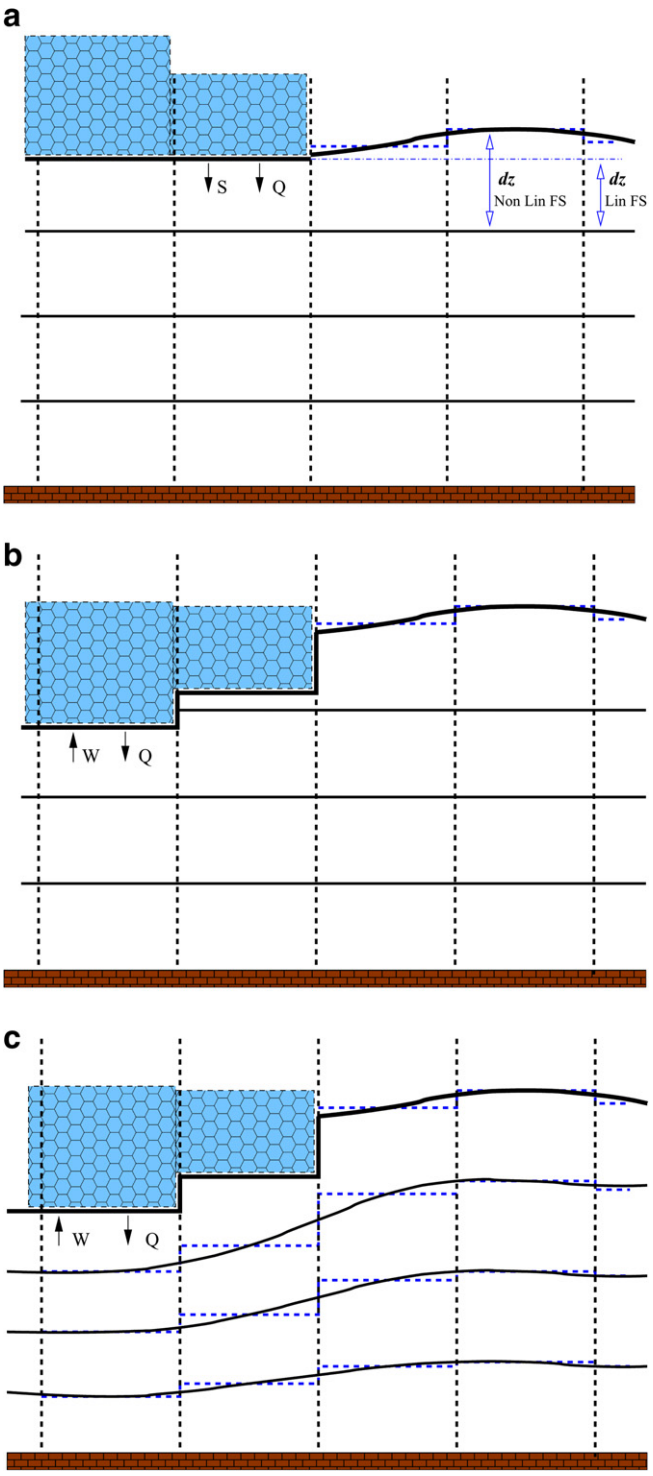

Fig. 1. Schematic view of three sea ice formulations: (a) no mass exchange (virtual salt flux); (b and c) real fresh water formulation (non-linear free-surface), in z-coordinates (b) and using z^*-coordinates (c). Heat flux (Q), and salt flux (S) in (a) or fresh-water flux (W) in (b and c), are represented by short arrows, corresponding to freezing conditions. Two open arrows in (a) represent the surface layer thickness $\mathrm{d}z$ which is used to compute oceanic advective fluxes, corresponding to the non-linear free-surface case $\mathrm{d}z = \Delta z_1 + \eta$ and the approximated linear free-surface case $\mathrm{d}z = \Delta z_1$. The sea-surface position is not affected by sea ice in (a) (so called "levitating" sea ice), but is depressed by the weight of sea ice in (b and c), with the first level empty in the left column of (b). The tilt of the coordinate in (c) avoids the problem of disappearing levels.

$$\frac{\partial \tilde{h}}{\partial t} \simeq -\nabla \cdot \int_{-H}^{\tilde{\eta}} \mathbf{u}_w \mathrm{d}z \tag{8}$$

$$\frac{\partial \tilde{h}\bar{S}}{\partial t} \simeq -\nabla \cdot \int_{-H}^{\tilde{\eta}} S\mathbf{u}_w \mathrm{d}z - S_s \cdot F_m/\rho_w + F_S/\rho_w \tag{9}$$

$$\frac{\partial \tilde{h}\bar{\theta}}{\partial t} \simeq -\nabla \cdot \int_{-H}^{\tilde{\eta}} \theta\mathbf{u}_w \mathrm{d}z - \theta_s \cdot F_m/\rho_w + F_H/(c_w\rho_w) \tag{10}$$

with θ_s being the surface temperature. The pressure term in ocean dynamics (4) simplifies to:

$$P_{hyd} = P_{z=\tilde{\eta}} + \int_z^{\tilde{\eta}} \rho g \mathrm{d}z \quad \text{with } P_{z=\tilde{\eta}} = P_{atm} \tag{11}$$

Some of the implication of the "virtual salt flux" approximation are summarized hereafter:

(a) Virtual salt-flux accuracy. Without a significant net global fresh-water flux ($\int\int F_m \mathrm{d}A \simeq 0$, which is generally the case), the barotropic dynamics will adjust quickly and ensure that $h \simeq \tilde{h}$, so that the term in Eq. (7) which is neglected here, $(\tilde{h}-h)\partial S/\partial t$, will remain small and the virtual salt flux $-S_s \cdot F_m/\rho_w$ will accurately represent the local dilution/concentration effect. On the other hand, when the fresh-water flux is not globally balanced over a long period, as in climate change scenarios, the virtual salt flux formulation holds mean sea-level constant, making analysis and interpretation less straightforward.

(b) Salinity conservation. Global conservation of salinity which should replace the conservation of the total amount of salt in the real fresh-water flux formulation, is no longer satisfied. For instance, in the case of no net global fresh-water flux, the global mean salinity is expected to remain constant. However, because of horizontal variations in the local surface salinity S_s, which are generally anti-correlated with fresh-water flux (higher surface salinity in evaporative regions, $F_m < 0$, and lower salinity in regions of excess precipitation, $F_m > 0$), $\int\int S_s \cdot F_m \mathrm{d}A < 0$, even if $\int\int F_m \mathrm{d}A = 0$; thus the global salinity will drift away. The magnitude of this salt loss can be estimated from climatological data sets: using a globally balanced fresh-water flux, the net salt imbalance is about $\sim -1.610^{-5}$ g/m^2/s, resulting in a global mean salinity drift of ~ -0.14 psu per 1000 years of simulation.[5] A possible remedy to this conservation problem is to evaluate the virtual salt flux using a uniform salinity S_o instead of the local surface salinity S_s, leading to a far less accurate representation of the dilution effect, which, for example, can be responsible for negative salinity in regions of large river outflow (Griffies et al., 2005).

(c) Inaccurate velocity to mass transport relation. Since the column thickness is left unaffected by the overlying sea ice, the horizontal oceanic mass transport is overestimated by an amount of the order of the sea ice transport, assuming comparable velocities. In thick ice-covered regions, part of the advantages of the non-linear free surface, which consists in a more accurate representation of mass transport, is lost. However, since the model dynamics generally compensates by adjusting the oceanic velocities, the mass transport is not affected significantly, and the inaccuracy and differences are more likely to be found in the velocities. This is confirmed in Section 3 analysis.

(d) Ice dynamics effects on oceanic variability. The divergence of the ice transport modifies the ice-loading field which affects the oceanic pressure, on the contrary to melting or freezing (which have no effects on oceanic pressure). The virtual salt-flux approximation with no ice-loading (Eq. (11)) ignores this effect, although the divergence of the oceanic transport might compensate in the special case where sea ice and ocean velocities are identical. On the other hand, sea ice and ocean velocities are rarely identical, in particular when the response to high frequency wind forcing is considered; and through the ice-loading coupling, sea ice dynamics can represent a significant source of oceanic variability, specially near the ice-edge where ice divergence/convergence is large; Section 3.2 illustrates this aspect.

(e) Barotropic dynamics. Another important missing aspect in this virtual salt-flux approximation is the dynamical effect of the fresh water flux, known as the Goldsbrough–Stommel circulation (Stommel, 1984). Although different intermediate formulations have been proposed to incorporate this effect, in rigid-lid model (Huang, 1993) or linear free-surface model (Tartinville et al., 2001), one must convert fresh water to an equivalent salt flux, since the column thickness, which is relevant for tracers, is held fixed.

2.3. Implications for sea ice dynamics

With regard to ice dynamics and ignoring sea ice loading, pressure forces are generally expressed as a sea-surface slope (see e.g., Hibler, 1979):

$$M_i \partial \mathbf{u}_i/\partial t = -h_i \nabla P_{atm} - M_i g \nabla \eta + [\text{Coriolis, Stress}] \tag{12}$$

where h_i, M_i are respectively the sea ice thickness and mass and $\mathbf{u}_i$ is the sea ice velocity. Although the atmospheric pressure gradient is a relatively small term, it has been added here to ensure consistency with ocean dynamics: it is important to account for the same forcing in both media (either to neglect atmospheric pressure in both, or to include it in both). This may be particularly important at low frequency since the ocean will adjust to atmospheric pressure loading (the inverse barometric effect).

When sea ice loading is accounted for, the sea-surface slope to consider is no longer the gradient of the mean ocean surface height (η) but becomes the gradient of the equivalent open water surface position η^{leads}, as defined in Section 2.1, and the second term on the right-hand-side of Eq. (12) reads: $-M_i g \nabla \eta^{leads} = -M_i g \nabla([\eta] + [M]_{(ice+snow)}/\rho_w)$.

This can be easily derived by considering the external pressure induced by horizontal forces acting on an ice-float of thickness h_i, from $z = \eta$ to $z = \eta + h_i$; below the floating line located at $z = \eta^{leads}$, the external pressure $P(z)$ is equal to the oceanic hydrostatic pressure: $P(z < \eta^{leads}) = P_{atm} + \rho_w g(\eta^{leads} - z)$ whereas above it, only atmospheric pressure remains: $P(z > \eta^{leads}) = P_{atm}$. Assuming a locally uniform sea-water density ρ_w, the vertically integrated horizontal pressure gradient can be written as:

$$\begin{aligned}\int_\eta^{\eta+h_i} \nabla P(z)\mathrm{d}z &= \int_\eta^{\eta+h_i} \nabla P_{atm}\mathrm{d}z + \int_\eta^{\eta^{leads}} \nabla(\rho_w g(\eta^{leads} - z))\mathrm{d}z \\ &= h_i \nabla P_{atm} + (\eta^{leads} - \eta)\rho_w g \nabla \eta^{leads}\end{aligned}$$

which allows one to recover the modified Eq. (12), since $M_i = (\eta^{leads} - \eta)\rho_w$.

2.4. A way forward using z^*

The z^* coordinate approach is an unapproximated, non-linear free surface implementation which allows one to deal with large amplitude free-surface variations relative to the vertical resolution (Adcroft and Campin, 2004). In the z^* formulation, the variation of the column thickness due to sea-surface undulations is not concentrated in the surface level, as in the z-coordinate formulation, but is equally distributed over the full water column. Thus vertical levels naturally follow sea-surface variations, with a linear attenuation with depth, as illustrated by Fig. 1c. Note that with a flat bottom, such as in Fig. 1c, the bottom-following σ_z coordinate and z^* are equivalent.

[5] Similarly, the heat loss can be estimated to be around 0.2 W/m^2 or equivalent to -0.5 K/kyr.

The definition and modified oceanic equations for the rescaled vertical coordinate "z^*", including the treatment of fresh-water flux at the surface, are detailed in Adcroft and Campin (2004). The major points are summarized here. Using the "$*$" notation to distinguish variables and expressions evaluated in the z^* vertical coordinate system rather than in the familiar z-coordinate, the position (z^*) and vertical discretization (Δz^*) are expressed as:

$$H + z^* = (H + z)/r \quad \text{and} \quad \Delta z^* = \Delta z/r \quad \text{with} \quad r = \frac{H+\eta}{H} \tag{13}$$

Since the vertical displacement of the free-surface is incorporated in the vertical coordinate z^*, the upper and lower boundaries are at fixed z^* position, $z^* = 0$ and $z^* = -H$, respectively. Also the divergence of the flow field is no longer zero as shown by the continuity equation:

$$\frac{\partial r}{\partial t} + \nabla_{z^*} \cdot (r\mathbf{u}_\mathrm{w}) + \frac{\partial}{\partial z^*}(rw^*) = 0 \tag{14}$$

where w^* represents the vertical velocity in the moving z^* coordinate which is related to the fixed frame vertical velocity w by the relation:

$$rw^* = rD_t(z^*) = w - (1 + z^*/H)D_t\eta + (\eta/H)(z^*/H)\mathbf{u}_\mathrm{w} \cdot \nabla H$$

with the time total derivative notation D_t.

The set of equations that must be solved is detailed in Adcroft and Campin (2004). Tracers (potential temperature, salinity, or a passive tracer) follow closely the continuity Eq. (14) and the main difference, compared to equations in height coordinate, appears in the horizontal momentum equation with a term related to the slope of the coordinate: with the density anomaly and hydrostatic pressure anomaly defined as $\rho' = \rho - \rho_\mathrm{w}$ and $p' = \int_z^\eta \rho g \mathrm{d}z$, the horizontal pressure gradient term in z-coordinates is replaced by

$$(g\nabla_z\eta + 1/\rho_\mathrm{w}\nabla_z p') \leftrightarrow g\nabla\eta + 1/\rho_\mathrm{w}\nabla_{z^*}p' + g(\rho'/\rho_\mathrm{w})\nabla_{z^*}[\eta(1+z^*/H)]$$

Interestingly, since z^* iso-surfaces are generally very close to horizontal surfaces, this slope term is generally small, even more when density anomaly is used as here. Problems related to pressure gradient errors, which are familiar to terrain following coordinate (σ), are thus not an issue here.

Constraints on minimum sea-level and maximum sea ice loading, which are severe in z-coordinates (Eq. (6)), are much less restrictive: what is required is that the thickness of the column be positive:

$$h = H + \eta = H + \eta^{\mathrm{leads}} - M_{\mathrm{ice+snow}}/\rho_\mathrm{w} > 0 \tag{15}$$

2.5. Time-stepping implementation

In this section, we set-out details of the implementation of sea ice with z^* in the MITgcm (Marshall et al., 1997a,b) using "real fresh water" boundary conditions and ice-loading effects. The time-stepping method has been identified as a crucial aspect for conservation of heat, salt and fresh water in non-linear free-surface ocean models (Griffies et al., 2001; Campin et al., 2004). Without sea ice, the fresh water flux is weakly coupled to heat flux (since the precipitation and run-off, which contains the largest high frequency variability, are uncoupled to heat or salt fluxes); in this case, a one time step delay between different component of the surface forcing is unlikely to cause problems, and details of the time-stepping of surface fluxes is not an issue. Sea-water freezing and sea ice melting are more demanding. Firstly, the implied heat flux (latent heat of freezing/melting) is a crucial component of the adjustment process of sea-surface temperature towards the freezing point. As a consequence, this heat flux needs to affect oceanic temperature without any delay to avoid any numerical stability problems. Secondly, the implied heat flux is also associated with significant fresh-water exchange (which is much larger than the evaporation analog since latent heat of melting is much smaller than latent heat of vaporisation). A consistent time-stepping treatment of heat and fresh-water fluxes is therefore desirable.

Most MITgcm applications use a staggering in time of density and momentum (staggered time-stepping) instead of a synchronous time stepping[6] since the former is more stable regarding internal mode dynamics. Staggered time-stepping is also commonly used in sea ice models, to advance in time sea ice dynamics, advection and sea ice thermodynamics (growth and melt); it is also used in the current model between sea ice and oceanic components. This allows one to, amongst other things, eliminate a one time step delay in the response to atmospheric forcing, oceanic mixed layer or sea ice thermodynamics, as sea ice is advected away or into a grid box. The resulting time-stepping appears as a sequence of (groups of) equations being advanced in time, one after the other.

The forward time-stepping sequence that is currently used in MITgcm is summarized in Fig. 2: sea ice is stepped forward in time in three separate stages, ice dynamics first, then sea ice advection and finally sea ice thermodynamics. The ice dynamics uses ice velocity ($\mathbf{u}_i^n$), ocean velocity ($\mathbf{u}_\mathrm{w}^n$), sea-surface (η^n), and ice-loading (M_ice^n) from the previous time step (subscript "n") and computes wind ($\tau_\mathrm{ai}^{n+1/2}$) and ice–ocean ($\tau_\mathrm{iw}^{n+1/2}$) stresses. The updated ice velocity ($\mathbf{u}_i^{n+1}$) is used to advect sea ice fields ($(\mathrm{ice})^*$, where "$*$" denotes an intermediate state). Sea ice thermodynamics results in a new sea ice state ($(\mathrm{Ice})^{n+1}$, subscript "$n+1$") and oceanic fluxes of fresh water ($F_\mathrm{m}^{n+1/2}$), salt ($F_\mathrm{S}^{n+1/2}$) and heat ($F_\mathrm{H}^{n+1/2}$). At this stage, all oceanic forcing are known and the momentum equations, including the continuity equation, are advanced in time: the explicit momentum tendency term ($\mathbf{G_u}$) are computed before solving the free-surface equation implicitly ($\eta^{n+1}, \mathbf{u}_\mathrm{w}^{n+1}$). And finally, using the recently updated flow field ($\mathbf{u}_\mathrm{w}^{n+1}$), the active tracers (potential temperature and salinity) are stepped forward (θ^{n+1}, S^{n+1}). Tracer conservation is exact, since level thickness (h^n, h^{n+1}) and surface forcing ($F_\mathrm{m}, F_\mathrm{H}, F_\mathrm{S}$) are consistent with the continuity equation.

The starting point is arbitrary, since the sequence is repeated in loops. Regarding the ordering of the three main blocks (sea ice, dynamics and thermodynamics), the only alternative ordering sequence is to permute dynamics and thermodynamics steps, which was the inherited choice in an earlier implementation of the non-linear free-surface (Campin et al., 2004). The difficulty of this alternative time-stepping lies in the synchronization of surface fluxes and thickness level between the continuity equation and tracer equation[7]; when sea ice coupling was introduced, the order was changed to this more natural time-stepping sequence.

Although melting and freezing modify the sea-surface position, they have no effect on oceanic pressure or dynamics. This is strictly the case in this time-stepping implementation, since melting reduces the ice loading (M_ice^{n+1}) and at the same time, adds the same amount of fresh water ($F_\mathrm{m}^{n+1/2}$). Without any ocean current anomaly, the fresh water flux induces, within the same time step, an increase of sea-surface elevation which exactly balances the reduction of ice-loading in the surface pressure term of the momentum equation.

[6] Both time-stepping methods are available in MITgcm, with the simple forward time-stepping or the Adams-Bashforth (second or third order) time-stepping options. However, depending on the advection scheme used for temperature and salinity, some option combinations might not be stable, thus limiting the effective choice.

[7] When thermodynamics is stepped forward just after the sea ice model, which provides the final surface fluxes, heat and salt fluxes are ready to be added to the right-hand-side of θ and S equations, and need to be incorporated directly for stability reason, as mentioned above. However, the fresh-water mass flux will only affects the next time step column thickness, after solving for the continuity equation at the end of the dynamics block.

External Forcing

Sea-Ice: Dynamics
$$\leftarrow \mathbf{u}_w^n\ ,\ M_{ice}^n\ ,\ \eta^n\ ,\ P_{atm}\ ,\ (Wind)^{n+1/2}$$
$$\rightarrow \mathbf{u}_i^{n+1}\ ,\ \tau_{ai}^{n+1/2}\ ,\ \tau_{iw}^{n+1/2}$$

Advection
$$\rightarrow (Ice)^*$$

Thermodynamics
$$\rightarrow (Ice)^{n+1}\ ,\ F_m^{n+1/2}\ ,\ F_H^{n+1/2}\ ,\ F_S^{n+1/2}$$

Dynamics:
$$\leftarrow \tau_{iw}^{n+1/2}\ ,\ F_m^{n+1/2}\ ,\ M_{ice}^{n+1}\ ,\ \eta^n\ ,\ P_{atm}\ ,\ \rho(\theta^n, S^n, p)$$
$$\rightarrow \mathbf{G_u}\ ,\ \mathbf{u}_w^* = \mathbf{u}_w^n + \Delta t \mathbf{G_u}$$
$$\rightarrow \eta^{n+1}\ ,\ \mathbf{u}_w^{n+1} = \mathbf{u}_w^* - \Delta t \nabla g \eta^{n+1}$$
$$\rightarrow h^{n+1} = h^n - \Delta t \nabla \cdot h^n \mathbf{u}_w^{n+1} + \Delta t F_m^{n+1/2}/\rho_w\ ,\ w^{n+1}$$

Thermodynamics:
$$\rightarrow (h\theta)^{n+1} = (h\theta)^n - \Delta t \nabla \cdot h^n \theta^n \mathbf{u}_w^{n+1} + \Delta t F_H^{n+1/2}/(\rho_w c_w)$$
$$\rightarrow (hS)^{n+1} = (hS)^n - \Delta t \nabla \cdot h^n S^n \mathbf{u}_w^{n+1} + \Delta t F_S^{n+1/2}/\rho_w$$

Fig. 2. Sketch of time-stepping sequence: the time-stepping comprises a sequence of partial updates with a right arrow to indicate updated fields and a left arrow to indicate input fields used in the updating process. In addition to notations from Eqs. (1)–(5), (Wind), τ_{ai} and τ_{iw} represent, respectively, wind speed, wind stress over ice and stress between ice and water; (ice) represents all sea ice state variables and $\mathbf{G_u}$ is the oceanic momentum tendency.

Some numerical instabilities in ice–ocean coupled dynamics have been reported (Schmidt et al., 2004) when mass exchange and ice-loading are accounted for. The implementation used in MITgcm did not show any dynamical instabilities. The time-stepping method might be one reason: the free-surface backward time-stepping scheme tends to damp the fastest, unresolved modes, and has a stabilizing effect. It is likely to adjust smoothly to the newly updated sea ice loading (M_{ice}^{n+1}) which contributes to the right-hand-side of the implicit free-surface equation. Another reason might be the horizontal discretization on the Arakawa-C grid, which is used both in the sea ice model and in ocean model, and is known to behave well in this type of situation.

3. Tests of an implementation of sea ice using z^* in a high resolution ocean model

Here we test out the MITgcm z^* implementation of sea ice–ocean mass exchange employing a non-linear free-surface. An extensive description of the model (Marshall et al., 1997a,b) is available on-line (MITgcm, 2002) and a summary of MITgcm recent developments can be found in Adcroft et al. (2004b). We presents results from a high resolution simulation including ice dynamics and high frequency forcing, which is particularly demanding in terms of numerical stability. This example addresses potential numerical instabilities related to ice dynamics and mass exchange coupling that have been reported by, for example, Schmidt et al. (2004).

3.1. 'Realistic' simulations

The simulations presented here are part of the ECCO_2 (Estimating the Circulation and Climate of the Ocean) project (Menemenlis et al., 2005). A cubed sphere grid (Adcroft et al., 2004a) with 510 grid points on the edge of each face provides relatively uniform resolution of 1/6° at the equator, and allows the use of a 20 min time step. The z^* coordinate (Adcroft and Campin, 2004) is employed with 50 layers whose thickness increases with depth, from 10 m at the surface to 450 m at 6 km. Vertical mixing is computed from the K-profile parametrization (KPP) (Large et al., 1994). The sea ice model computes ice thickness, ice concentration and snow cover (Zhang et al., 1998) and solves viscous-plastic ice rheology using the Zhang and Hibler (1997) algorithm. The 6 hourly NCEP reanalysis of wind, air temperature and humidity and short-wave and long-wave downward radiation are used to calculate atmospheric forcing through bulk-formulae.

Ocean currents at the second level, corresponding to a depth of approximately 15 m, are shown in Fig. 3 on the native model cubed sphere grid, from September 12 of the last year of a 10 years integration, similar to the control simulation (see details below). Although the horizontal resolution in mid and high-latitudes is relatively coarse to adequately resolve the eddy length scale, the meso-scale eddy field is clearly well developed and qualitatively match the observed SSH variability.

Two simulations, each of 3 years duration, were performed:

(1) The 'control' experiment uses 'levitating ice' as in Fig. 1a, ignores the mass flux exchange at the ocean upper surface and converts fresh-water flux into virtual salt-flux (salt-flux formulation). This is a commonly used implementation in z-coordinate models.
(2) The 'ice-loading' experiment fully accounts for ice loading and mass flux exchange with the atmosphere and between ocean and sea ice.

Those are the only differences between the two simulations, and other parameters, forcing and initial state are strictly identical. For convenience, both experiments use a non-linear free-surface employing a z^* coordinate.

Sea ice is locally thicker in the Arctic region than in the Southern hemisphere and so we choose to focus on the Northern hemisphere polar region where ice-loading will be consequently larger. The simulated sea ice distribution (sea ice fraction) is represented over the north face of the cube-sphere grid,[8] at the time of maximum ice extent (March 10th) and the time of minimum ice extent (September 6th). The black contour represents the fifty percent ice concentration from the SSMI satellite and allows one to assess the skill of the simulation. In winter (Fig. 4a), the model notably

[8] This mapping is in fact very similar to a polar projection at high-latitudes.

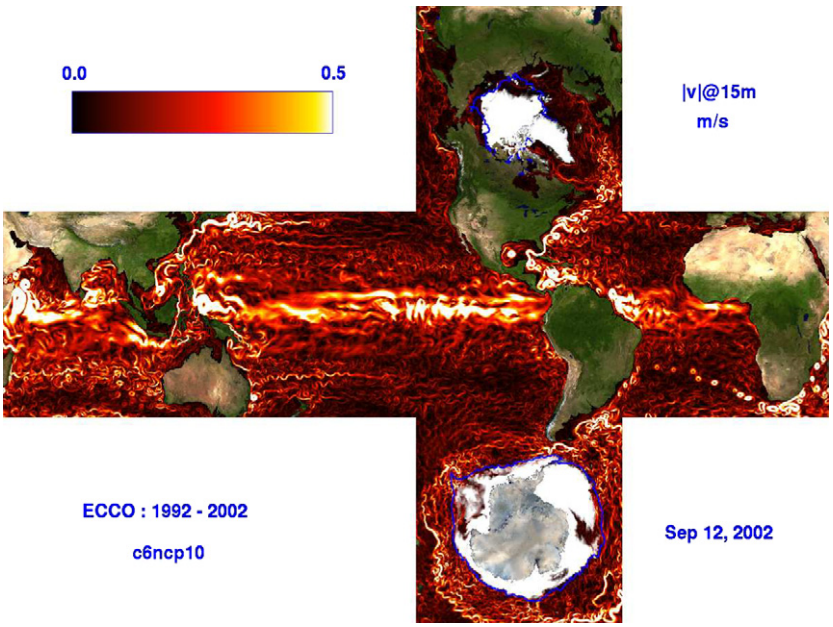

Fig. 3. Fields are presented at the end of 10 years of integration (September 12, 2002) of a global eddy resolving on the cubed sphere at resolution CS-510: ocean velocity at 15 m depth is represented in color on the native CS-510 model grid. White areas designate the presence of sea ice. The blue contour indicates the 50% sea ice concentration from satellite observations (SMMR-SSMI).

reproduces the position of the ice-edge in the Bering and Okhotsk seas, as well as in the Greenland and Barents Seas, but slightly underestimates sea ice cover in the Labrador Sea and the Great Banks area (South-East of Newfoundland). The model also captures the retreat of the ice in summer (Fig. 4b), especially in the Greenland Sea, the Barents Sea and in the coastal area North of Siberia. It is pleasing to see the model maintaining sea ice in the East Siberian Sea (or Chukchi Sea) as observed. However, too much sea ice remains in the Baffin bay, in the Canadian Archipelago and near the coast in the Beaufort Sea. One also observes a reduction of ice concentration down to 60–70% over a large area of the central Arctic ocean at the end of the melting season, which is not obviously evident in the satellite measurements.

3.2. Analysis of ice-loading effects

The comparison of the two simulations reveals that the sea ice fields are very similar, as are almost all oceanic diagnostics. Given the high intrinsic variability of the currents, longer integrations would be necessary to derive statistically significant differences. For example, the Goldsbrough–Stommel circulation (typical magnitude < 1 Sv, see: Roullet and Madec, 2000, their Fig. 4a), which ought to manifest itself as a difference in the vertically integrated transport between the two experiments (not shown), is dominated by the footprint of eddies which induce differences which are 1 or 2 orders of magnitude larger.

Differences between the control and ice-loading experiments are most evident, not surprisingly, in the SSH. Fig. 5 illustrates several diagnostics of SSH from the two experiments, both averaged over a winter month (March 1994) when sea ice, and especially sea ice dynamics, have the largest impact. The mean SSH is represented in color in Fig. 5a and c with four ice thickness contour lines of increasing thickness (at 0.1 m, 0.3 m, 1 m and 3 m).

Sea ice loading (Fig. 5c) strongly depresses the mean SSH down to 4 m below the reference sea-level North of Greenland, where sea ice is the thickest, in contrast to the control experiment (Fig. 5a) in which the monthly mean SSH in the Arctic ocean is uniformly around 1 m below sea-level with no associated gradient in sea ice thickness. This results in an "inverse barometric" effect[9], in which SSH rapidly adjusts to compensate for the surface pressure loading, so that no significant difference persists between the two in monthly mean diagnostics of ocean surface pressure or equivalent η^{leads} (not shown), except for the signature of eddy variability.

The monthly standard deviation of SSH in the control experiment (Fig. 5b) indicates high SSH variability in shallow, ice free regions such as in the North-Sea, which are also noticeable in the ice-loading experiment (Fig. 5d). The mesoscale eddy footprint on SSH standard deviation is much lower on time scales as short as 1 month, and can only be identified in the most active regions such as the mid-latitude North Atlantic sector (lower left corner of Fig. 5b and d). In contrast to the control run, the ice-loading experiment shows a much higher standard deviation of SSH (Fig. 5d) in ice-covered regions, especially along the sea ice margin where the largest values are found, such as in the southern part of the Greenland Sea (exceeding 0.5 m) and also near the Siberian coast.

The SSH variability associated with sea ice loading has different consequences on ocean dynamics: sea ice thermodynamics processes such as freezing and melting affect sea ice loading and contribute to SSH variability, but have no direct effects on ocean dynamics since the surface mass exchange exactly compensates (both physically and numerically) the ice-loading variations, leaving the ocean surface pressure unchanged. On the other hand, sea ice advection also affects sea ice loading and modifies ocean surface pressure. As a consequence, ocean dynamics responds to surface pressure variations, adjusting SSH and therefore contributing to SSH variability. This dynamical adjustment takes place whenever sea ice velocity and ocean currents are different from one-another, but must be neglected unless sea ice loading is taken in to account.

[9] No SSH dynamical adjustment is needed in the course of freezing and melting, if sea ice does not move. However, changes in ice loading due to sea ice advection are not locally balanced by a mass exchange at the ocean surface, and will therefore trigger an ocean dynamical response.

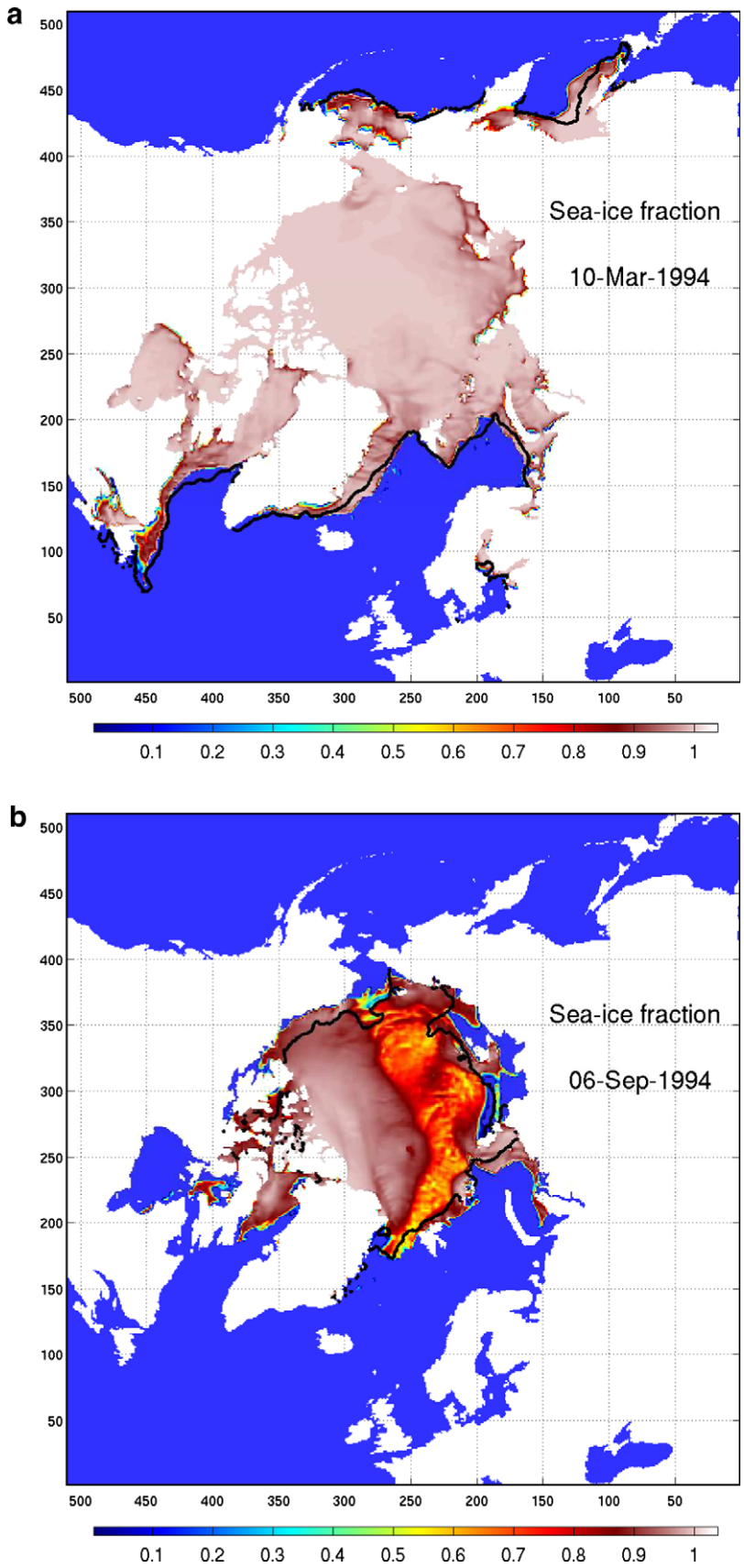

Fig. 4. Simulated sea ice fraction (in color), from the control experiment, corresponding to: (a) March 10, 1994; (b) September 6, 1994. Superimposed is the 50% ice concentration contour (black line) from satellite measurements.

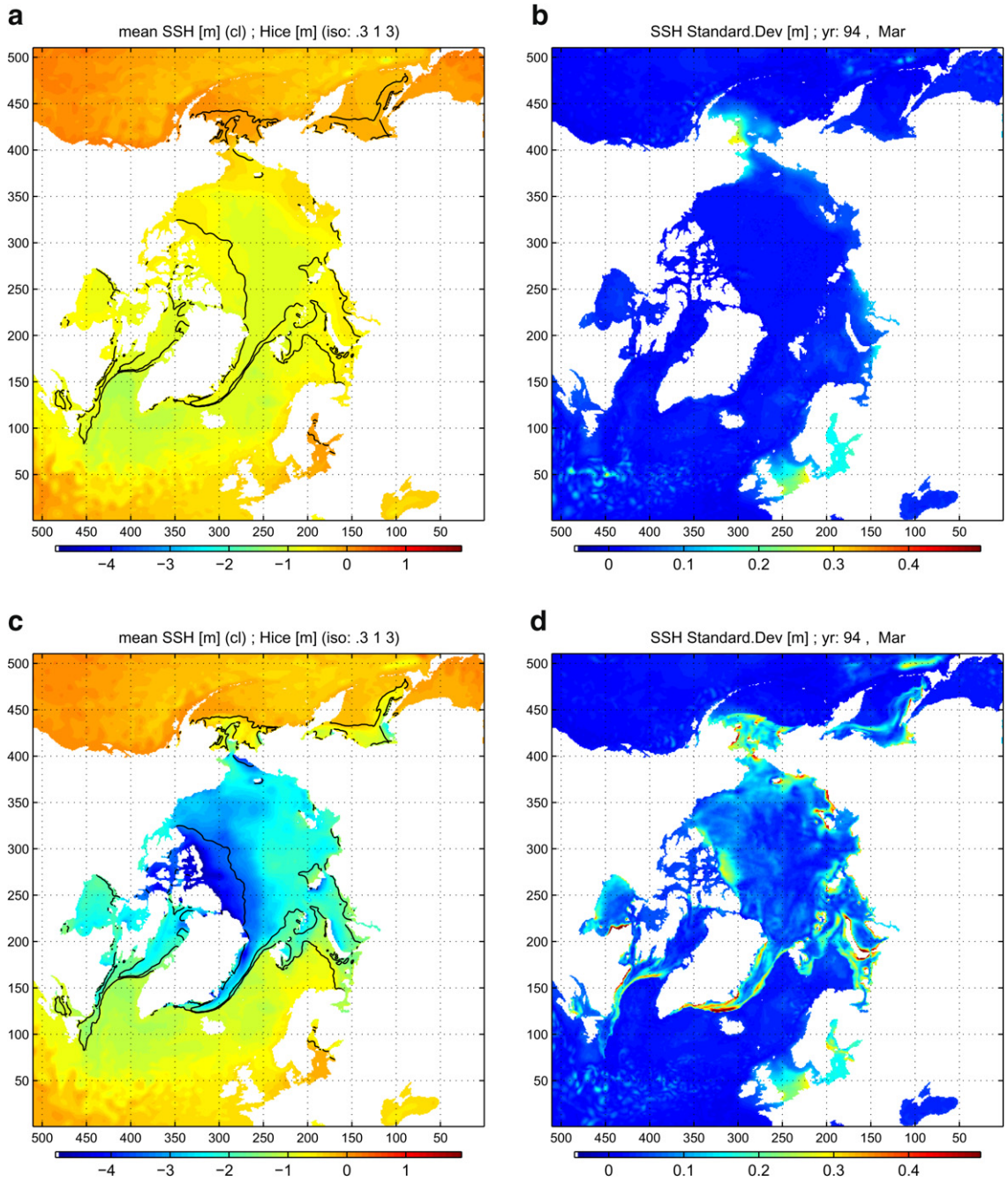

Fig. 5. (a) and (c) March 1994 monthly mean SSH (color) and sea ice thickness (lines: 0.1, 0.3, 1, 3 m). (b) and (d) March 1994 monthly standard deviation of SSH. The top 2 panels (a and b) are from the control experiment and the bottom 2 panels (c and d) from the ice-loading experiment. The same color scales are used to facilitate comparison.

We believe that most of the sea ice associated SSH variability, especially near the sea ice edge, is due to ice advection and little can be explained by sea ice thermodynamics alone: sea ice freezing and melting is rather slow (compared to the forcing period) and weak, especially during the months of maximum sea ice extent. In contrast, ice dynamics responds rapidly and strongly to high frequency wind forcing, even more so than ocean currents.[10] Therefore, we believe that most of the sea ice related SSH variability seen in Fig. 5d involves dynamical oceanic adjustment to wind-driven ice-loading variations; this source of oceanic high frequency variability is absent in the control experiment without ice-loading effects.

3.3. Evidence of model stability

In order to clarify the interpretation of the SSH standard deviation pattern, two different versions of SSH time derivative root-mean-square (RMS) have been computed, both from the same period (March 94) of the ice-loading simulation. The first one uses directly the unfiltered SSH time derivative from the model (time-step $= \Delta t = 20$ min) whereas the second one estimates the SSH time derivative from 6 hourly mean SSH

[10] Several factors contribute to the stronger and faster sea ice response to high frequency wind forcing compared to ocean surface currents: (1) the air drag coefficient is generally larger over sea ice than over open water; (2) under sea ice, a delay is expected from the ocean response to a rapid change in the wind since the momentum flux is passed to the ice, and then sea ice velocity generates ice–ocean stress which in turn drive ocean currents; (3) the inertia of a meter or so of sea ice is smaller than the 10. m surface ocean level, thus leading to a more rapid sea ice response.

($\Delta\tau = 6$ h = forcing period) thus filtering out the highest frequencies:

$$\left[\frac{\partial\eta}{\partial t}\right]^{\mathrm{RMS}}_{\Delta t} = \sqrt{\overline{(\Delta\eta/\Delta t)^2}^{\mathrm{month}}} \quad \text{and} \quad \left[\frac{\partial\eta}{\partial t}\right]^{\mathrm{RMS}}_{\Delta\tau} = \sqrt{\overline{(\Delta\overline{\eta}^{\tau}/\Delta\tau)^2}^{\mathrm{month}}}$$

The first diagnostics is plotted in Fig. 6a in units of cm/day and gives an indication of the full SSH variability resolved by the model at all frequencies. The ratio of the two diagnostics (second divided by the first) is plotted in Fig. 6b. It is a measure of the relative contribution of the variability at the forcing and longer frequencies, to the total variability.

The RMS SSH tendency including all frequencies (Fig. 6a) is much larger in the North-Sea and in the Bering Sea. This is a response to winter storm track activity in the North Atlantic and Pacific which becomes amplified in shallow regions (storm-surge like phenomena) and occurs mainly at the forcing frequency as indicated by Fig. 6b (RMS ratio very close to unity). At the ice-edge boundaries in the Greenland and Labrador Seas, the SSH standard deviation is large (Fig. 5b) and the variability seen in Fig. 6a, although weaker than in shallow seas, is also concentrated at the forcing frequency (see Fig. 6b). This can be understood in terms of the influence of wind forcing on sea ice dynamics and consequent ice-loading fluctuations. In other areas of the Arctic ocean, the RMS of SSH tendency is remarkably low (Fig. 6a), even in locations where the SSH standard deviation is significant (Fig. 5d) and therefore corresponds to low frequency variability relative to the forcing period.

The comparison of SSH variability at different frequencies is a good indicator of numerical noise and potential dynamical instability. Since the fastest oceanic response is barotropic and necessarily involves SSH adjustments, any dynamical instability will generate high frequency oscillations and therefore appear in the unfiltered RMS tendency but make little contribution to diagnostics based on the 6 hourly filtered fields. Such instability is therefore expected to produce a small RMS ratio of filtered versus unfiltered SSH tendencies in Fig. 6b. The central Arctic region reveals a few patches of lower variability ratio (50%, Fig. 6b) where the full variability (Fig. 6a) is extremely small, and therefore not significant. On the contrary, the ratio is very close to one at the ice-edge where the full variability is significant. In most sea ice-covered areas (Greenland sea, Bering Sea, Labrador Sea) the ratio is even higher than in the nearby open ocean; values of 70% in ice free regions are commonly found next to steep bottom slopes and could result from dynamical adjustment and interaction with topography. This comparison allows one to conclude that there is no sign of dynamical instability in our implementation of sea ice loading and sea ice–ocean mass exchange.

4. Test of conservation in an idealized coupled atmosphere, ocean, sea ice model

The objective of this second example is to illustrate the ability of a coupled model employing a rescaled vertical coordinate to conserve mass, heat and salt during extended climate integrations. The coupled model used here exploits an isomorphism between ocean and atmosphere dynamics (Marshall et al., 2004) allowing one to generate an AGCM and OGCM from the same modular MITgcm code. The two GCMs use specific physics packages but share the same hydrodynamical kernel using an isomorphic vertical coordinate: the rescaled pressure coordinate (p^*) for the compressible atmosphere, and rescaled height coordinate (z^*) for the Boussinesq ocean (Adcroft and Campin, 2004).

In particular, both models use the same cubed sphere grid (Adcroft et al., 2004a) at low resolution ($32 \times 32 \times 6$ faces, 2.8° resolution at the equator) which greatly simplifies the implementation of a conservative interface between the two GCMs. The computationally inexpensive atmospheric physics "SPEEDY" (Molteni, 2003) is used at low vertical resolution (5 levels). The sea ice model is based on the Winton (2000) two and half layer thermodynamic sea ice model. The prognostic variables are ice fraction, snow and ice thickness and a two-level sea ice enthalpy representation which accounts for brine pockets and sea ice salinity employing an energy conserving formulation. More details of the coupled model can be found in Marshall et al. (2007).

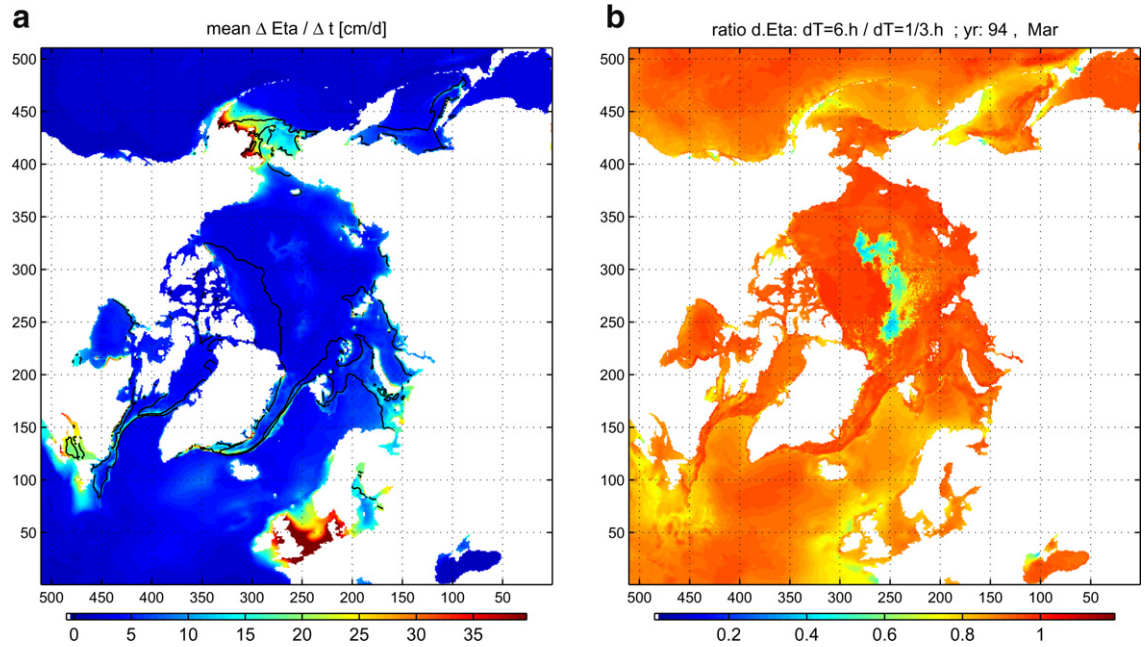

Fig. 6. March 1994 RMS sea-surface height time derivative [cm/d]: (a) sampled at the model time step ($\Delta\tau = \Delta t$) thus retaining all frequencies; (b) sampled at forcing period ($\Delta\tau = 6$ h) normalized that in panel (a).

Although our model can simulate an earth-like climate in a realistic configuration, including topography, bathymetry and land processes, here an idealized aqua-planet configuration has been selected since it simplifies diagnostics of global budgets because there is no land component[11] whilst retaining the sea ice–ocean interface, the focus of the present study. The model set-up and parameters are identical to the (Marshall et al., 2007) study, except that:

(1) An ocean of reduced depth in used (3. km instead of 5.2 km). This has the advantage of bringing the global ocean volume closer to the present value and reduces by almost a factor of 2 the time required to integrate the system to equilibrium.
(2) The number of vertical levels employed on the ocean model is increased from 15 to 25 levels with 10 m resolution near the surface and 7 levels in the top 100 m.
(3) The KPP vertical mixing scheme is employed (Large et al., 1994) rather than convective adjustment.
(4) Implicit treatment of internal gravity waves (Robert et al., 1972) enable the use of a longer atmospheric time step.

These changes affect the spin-up time scale but result in very little difference to the mean climatic state of the model that emerges after 1000 years of integration (see Marshall et al., 2007 for a description of the mean state).

The experiment presented hereafter is an adjustment after a crude restart in which the atmosphere and ocean are set to have zero winds and currents. The atmosphere is assumed to be dry and uniformly stratified: the ocean temperature and salinity structure is taken from a quasi-equilibrium coupled aqua-planet integration. Sea ice is assumed not be present in the initial state. With only the long term memory of the coupled system (temperature and salinity) as initial conditions, after a few hundred years of integration, the coupled model returns to its mean statistical equilibrium state. However, in the first 50 years of the adjustment period, the sea ice distribution develops a fascinating "donut" shape in both hemispheres, which, during the first 5 years, melts away in summer. Thereafter the sea ice "donut" becomes permanent until year 27, as illustrated in Fig. 7, and in subsequent years partially closes during the winter until disappearing completely after 50 years. A detailed analysis indicates that during the first winter, sea ice recovers almost the same area as that in the equilibrium state, leading to large sea ice formation in polar regions. The implied brine release is large enough to erode the polar halocline and to trigger deep mixing and convection at the poles. The presence of warmer water at depth ($\sim$ 200 m) provides a source of heat over the next few decades, which prevents sea ice from completely covering the poles. Over the open polar waters, strong atmospheric cooling and brine rejection sustain deep mixing during this period. The 5-year average (from years 5 to 10) zonal mean net heat fluxes from the ocean to the atmosphere is represented in Fig. 8 (top panel) and indicates larger heat loss at the pole, around 50 W/m^2, than on the equatorial flank of the sea ice ring (represented in color) (16 W/m^2, at 65°). In contrast, the isolating effect of the sea ice cover reduces the heat loss to only 8 W/m^2 at 75°. The persistent large-scale polynya at the two poles are simulated here without sea ice dynamics, but the involved mechanism resembles the one mentioned for the Antarctic region polynya (Morales Maqueda et al., 2004).

On yearly time scales, and since ice dynamics is not represented here, the surface net heat flux from ocean to atmosphere and the oceanic heat exchange at the base of the sea ice are not very different: the difference is plotted in Fig. 8 (bottom panel, dashed blue line) and does not exceed 4 W/m^2 over a 5-year period. It matches exactly, to machine precision, the heat storage in the sea ice and snow cover (red line), thus confirming the excellent conservation of heat at the ocean sea ice-atmosphere interfaces.

A similar diagnostic for fresh water can be derived. The 5-year average (years 5–10) zonally integrated meridional transport in the ocean (Fig. 9 bottom panel) has been integrated on the native model grid, from the bottom to the top, taking into account the time-varying grid cell thickness of the z^* coordinate. The stream-function at the surface (top panel, red line) does not vanish but is very close to the integrated fresh-water flux at the surface (blue line). A perfect match is obtained when the sea-level storage term $\partial\eta/\partial dt$ (dashed blue line) is added to the fresh-water flux, with residual differences of less than 10^{-13} Sv, the precision of the machine.

[11] The simple land-component and run-off scheme conserve fresh water and heat; however, continental ice is not yet accounted for in the present model. And in general, storage over land that involves very different time scales complicates global budgets.

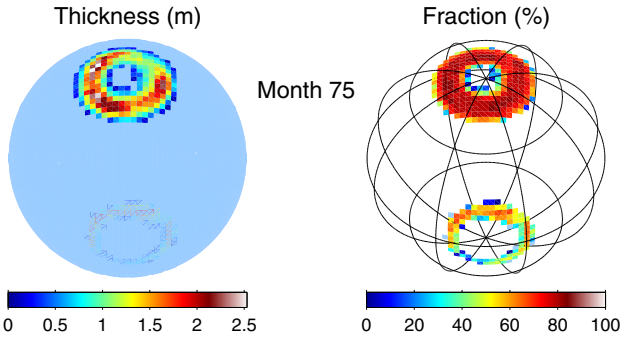

Fig. 7. Thickness (in m) and sea ice fraction on the 75th month (March) of a coupled integration. An animation covering the first 50 years of integration can be viewed from http://mitgcm.org/movies/Sea_Ice_Donut_x1.mpg.

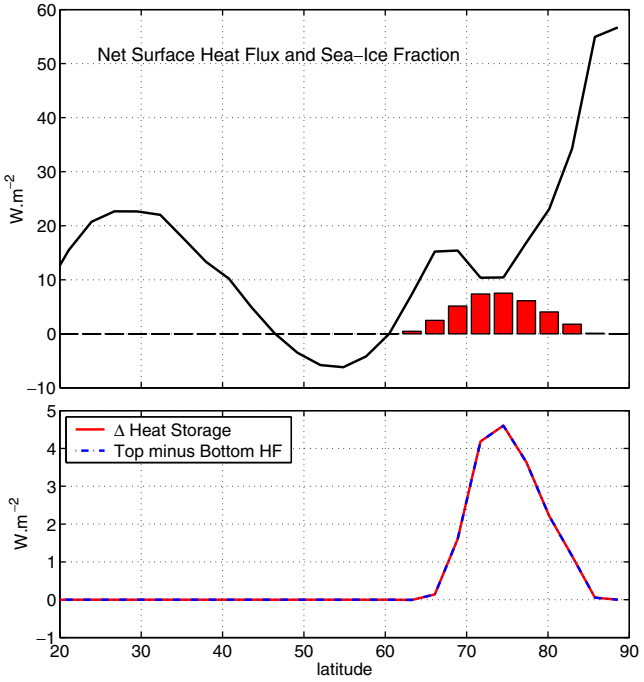

Fig. 8. Top: latitudinal dependence of zonally average surface heat flux (W/m^2, left axis); the zonal mean sea ice fraction has been added in red on a 10 times smaller scale. Bottom: zonally averaged heat budget of the sea ice, as a function of latitude: the heat storage (in red) perfectly matches the integrated heating rate (dashed blue line) computed from the difference between top and bottom heat flux. All quantities are 5-year averages corresponding to years 5–10.

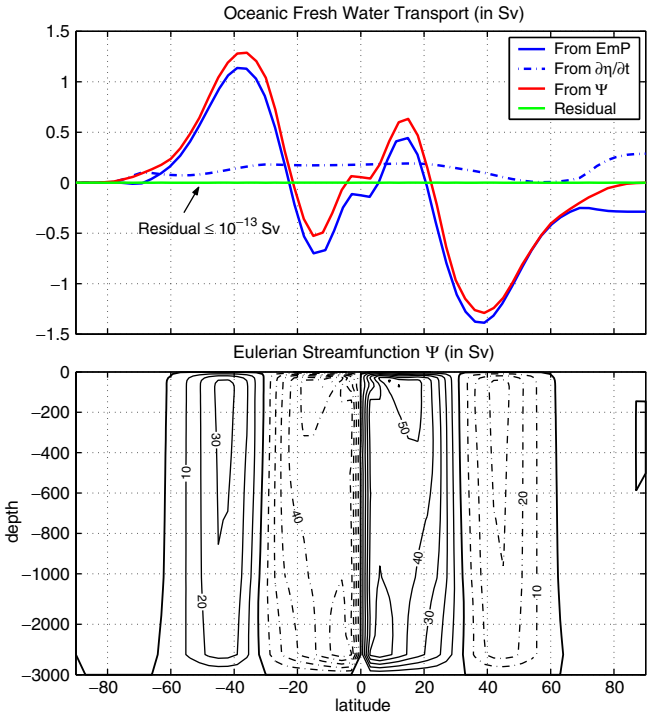

Fig. 9. Bottom: oceanic meridional overturning stream-function (in *Sv*), average over 5 years. the stream-function is non-zero at the surface (top panel) as a result of integrating the meridional transport upwards, from the bottom to the top. Top panel: oceanic stream-function at the surface (red line), area integrated fresh-water flux (blue line) and area integrated sea-level change (dashed blue line); the green line represent the residual: $\Psi - \mathrm{EmP} - \partial\eta/\partial t$.

In addition to fluxes and transport, the evolution of mean sea-level, heat content or salt content can also be compared to the time integrated associated surface flux, and is an even more precise indicator of any small drift or inaccuracy that might accumulate over time. Such diagnostics are discussed hereafter.

The time integrated atmospheric fresh-water flux (P–E, Fig. 10a, black line) drops rapidly but then remains remarkably constant, representing the initial moistening of the atmosphere, which is initialized from a completely dry state. Thereafter the atmosphere takes on a relatively constant 'head' of water vapor. In contrast, the sea ice and ocean fresh water content (Fig. 10a, blue and green line) can be seen drifting in the opposite direction, corresponding to a global increase of sea ice and snow storage. A double seasonal cycle in sea ice volume can be identified in the first years of integration (Fig. 10a) but is subsequently strongly damped when ice volume steadily grows after year 5. As expected, the integrated fresh-water flux into the ocean (and below sea ice where sea ice is present) (Fig. 10a, in red) matches well the evolution of sea-level (in green). Simply by subtracting the incoming time integrated fresh-water flux from the fresh-water content (Fig. 10b), one can check the accuracy of the fresh-water conservation over the 50 years of integration, for the ocean component (red line), the sea ice component (blue line) or the combination of the two (black line). In all cases, the residual is of the order of the machine precision ($\sim 10^{-12}$ kg/m^2) when compared to the magnitude of local variations (~ 1000 kg/m^2 ~ 1 m of sea-level).

The time integrated salt budget (not shown) is somewhat simpler, since it involves only sea ice (with constant salinity) and the oceanic component. It has similar levels of conservation with residuals of the order of $\sim 10^{-7}$g/m^2, close to the machine precision when compared to a typical water column salt content ($\sim 10^{8}$g/m^2).

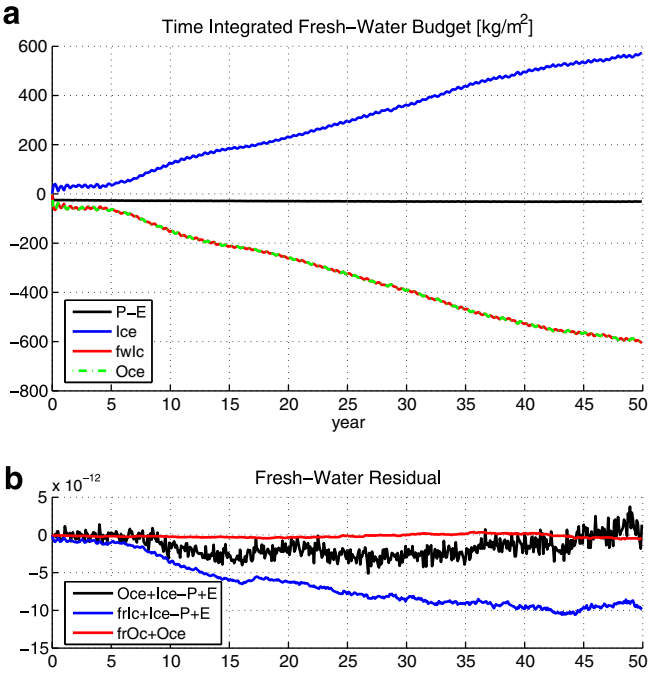

Fig. 10. (a) Global mean, time integrated fresh-water budget, in units of kg/m^2: from the atmosphere (P–E, black line), at ocean surface below sea ice (red line), evolution of the sea ice fresh water content (blue line) and evolution of the mean sea-level (green dashed line). (b) Residuals derived from panel (a): the sum of E–P, ice content and sea-level (black line); the sum of E–P, flux below sea ice, and ice content (blue line) and the ocean sea-level plus flux below sea ice (red line).

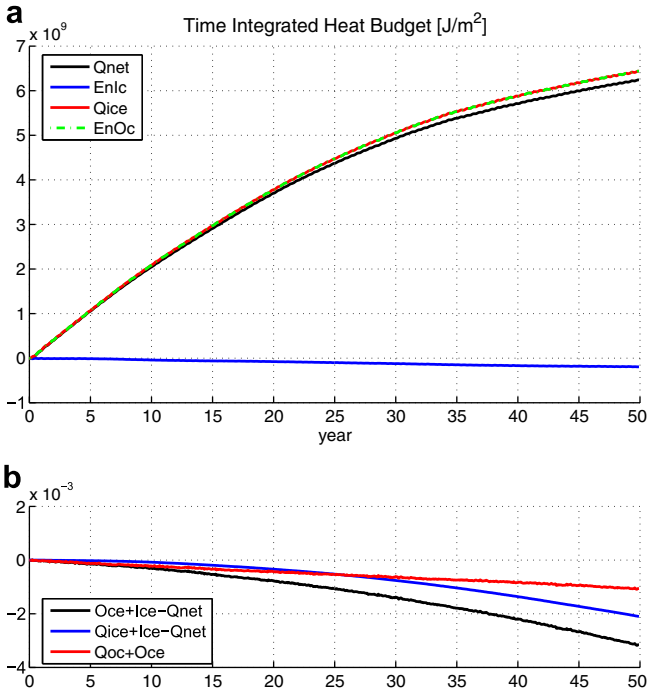

Fig. 11. (a) Global mean, time integrated heat budget, in units of J/m^2: net heat flux from the atmosphere (black line, Qnet), at ocean surface below sea ice (red line, Qice), evolution of the sea ice (blue line) and oceanic (green dashed line) heat content anomaly from the initial state; (b) residuals derived from panel (a): the sum of oceanic and ice heat content, minus atmospheric Qnet (black line); the sum of Qice flux and ice content, minus atmospheric Qnet (blue line); the sum of Qice and ocean heat content (red line).

The time integrated heat budget (Fig. 11) shows a larger dis-equilibrium than its salt and fresh-water counter-parts: the atmo-

spheric net surface heat flux (black line), the oceanic surface heat flux (red line) and the oceanic heat content (green line) all indicate a relatively large oceanic warming which slowly diminishes toward the end of the 50 years simulation, but remains much larger than the sea ice heat storage term (blue line). The coupled system is subject to radiative fluxes at the top, which are not balanced in this adjustment experiment: compared to the quasi-equilibrium state from which the initial oceanic temperature is taken, and to where the coupled model is returning over time, the planetary albedo is lower because of reduced sea ice and snow cover extent. This explains the significant early warming phase which attenuates after 25–30 years of simulation, as the sea ice cover increases along with the planetary albedo.

The accuracy to which heat is conserved (Fig. 11b), for the ocean component (red line), the sea ice component (blue line) or the combination of the two (black line) is again limited by machine precision, and exhibits residuals of the order of 10^{-3} J/m^2 when compared to the typical water column heat content ($\sim 10^{11}$ J/m^2).

The perfect conservation of heat, salt and fresh water demonstrated in these coupled experiment, is a consequence of the use of the non-linear free formulation which provides a natural and conservative way of dealing with free-surface undulations and fresh-water mass exchange in tracer budgets (Campin et al., 2004). However, in applications where sea ice can become rather thick near the poles, and thicker than the vertical resolution at the surface (10 m in this case), the rescaled vertical coordinate z^* becomes essential since it allows mass exchange and its related ice-loading formulation to be used without vertical resolution limitations near the surface.

5. Conclusions

The rescaled vertical coordinate z^* allows one to fully account for fresh-water mass exchange between sea ice and ocean and the resulting sea ice loading acting at the top of the ocean column. In particular, the z^* formulation avoids the problem of surface levels disappearing under thick sea ice loading even when modest vertical resolution is used.

Sea ice and the upper ocean are strongly coupled because of freezing and melting. But in addition to this thermodynamical coupling, the sea ice loading strengthens the dynamical coupling between the two components. Thus places special demands on the time-stepping methods employed in coupled sea ice–ocean model required to ensure numerical stability. The detailed time-stepping implementation described here proves to be stable and conservative.

Two radically different set-ups were used to illustrate the successful implementation of mass exchange and ice-loading with z^* coordinate.

The non-linear free-surface provides a natural and conservative way of dealing with free-surface undulations and tracer budgets which account for free-surface induced column thickness variations in the tracer budget (Campin et al., 2004). The z^* formulation inherits from this free-surface implementation and demonstrates perfect conservation of fresh-water heat and salt in an idealized configuration of the coupled atmosphere sea ice–ocean MITgcm model. This endows the coupled model with a crucial advantage for long term integrations.

The ice-loading dynamical effects are analyzed in a high resolution z^* coordinate global ocean sea ice model, and do not show any sign of instability despite use of a reasonably long time step. The sea ice dynamics responds rapidly to high frequency wind forcing, and generates high frequency oceanic variability, which is neglected unless sea ice loading is accounted for. Although this source of oceanic variability is significant at the forcing frequency, and tends to dominate near the ice-edge front, its relative importance would need to be addressed by comparing with other sources of barotropic forcing such as tides (absent in our simulations).

Among other applications that can benefit from the z^* coordinate formulation, the explicit representation of barotropic tides in OGCMs is certainly a major one, as illustrated by (Adcroft and Campin, 2004). With growing interest in tides – sea ice interactions (e.g. (Hibler, 2006)), a significant improvement can be expected from the z^* coordinate with realistic sea ice loading effects interacting with oceanic tides and sea ice dynamics. This will be the subject of future papers.

Acknowledgements

We wish to thank Gavin Schmidt and an anonymous reviewer for constructive comments that improved the manuscript. We are thankful to Dimitris Menemenlis and Chris Hill for helping with high resolution simulations. This study was supported by a grant from ONR and NASA (ECCO-2).

References

Adcroft, A., Campin, J.-M., 2004. Re-scaled height coordinates for accurate representation of free-surface flows in ocean circulation models. Ocean Modelling 7, 269–284.

Adcroft, A., Campin, J.-M., Hill, C., Marshall, J., 2004a. Implementation of an atmosphere-ocean general circulation model on the expanded spherical cube. Monthly Weather Review 132, 2845–2863.

Adcroft, A., Hill, C., Campin, J.-M., Marshall, J., Heimbach, P., 2004b. Overview of the formulation and numerics of the MIT GCM. In: Proceedings of the ECMWF Seminar Series on Numerical Methods, Recent Developments in Numerical Methods for Atmosphere and Ocean Modelling, pp. 139–149.

Bleck, R., 2002. An oceanic general circulation model framed in hybrid isopycnic-cartesian coordinates. Ocean Modelling 4, 55–88.

Campin, J.-M., Adcroft, A., Hill, C., Marshall, J., 2004. Conservation of properties in a free-surface model. Ocean Modelling 6, 221–244.

Griffies, S., Gnanadesikan, A., Dixon, K.W., Dunne, J.P., Gerdes, R., Harrison, M.J., Rosati, A., Russell, J.L., Samuels, B.L., Spelman, M.J., Winton, M., Zhang, R., 2005. Formulation of an ocean model for global climate simulations. Ocean Science 1, 45–79.

Griffies, S., Pacanowski, R., Schmidt, M., Balaji, V., 2001. Tracer conservation with an explicit free surface method for z-coordinate ocean models. Monthly Weather Review 129, 1081–1098.

Hibler III, W.D., 1979. A dynamic thermodynamic sea ice model. Journal of Physical Oceanography 9, 815–845.

Hibler III, W.D., 2006. Influence of oceanic tides on sea ice thickness variability. Eos Trans. AGU 87(52) (Fall Meet. Suppl.), Abstract C31B–35.

Holland, D., Jenkins, A., 2001. Adaptation of an isopycnic coordinate ocean model for the study of circulation beneath ice shelves. Monthly Weather Review 129, 1905–1927.

Huang, R.X., 1993. Real freshwater flux as a natural boundary condition for the salinity balance and thermohaline circulation forced by evaporation and precipitation. Journal of Physical Oceanography 23, 2428–2446.

Jenkins, A., Hellmer, H., Holland, D., 2001. The role of meltwater advection in the formulation of conservative boundary conditions at an ice-ocean interface. Journal of Physical Oceanography 31, 285–296.

Johns, T.C. et al., 2006. The new Hadley Centre climate model (HadGEM1): evaluation of coupled simulations. Journal Climate 19, 1327–1353.

Large, W., McWilliams, J., Doney, S., 1994. Oceanic vertical mixing: a review and a model with nonlocal boundary layer parameterization. Review in Geophysics 32, 363–403.

Marshall, J., Adcroft, A., Campin, J.-M., Hill, C., White, A., 2004. Atmosphere-ocean modelling exploiting fluid isomorphisms. Monthly Weather Review 132, 2882–2894.

Marshall, J., Adcroft, A., Hill, C., Perelman, L., Heisey, C., 1997a. A finite-volume, incompressible Navier Stokes model for studies of the ocean on parallel computers. Journal of Geophysical Research 102, 5753–5766.

Marshall, J., Ferreira, D., Campin, J.-M., Enderton, D., 2007. Mean climate and variability of the atmosphere and ocean on an aqua-planet. Journal of the Atmospheric Sciences 64, 4270–4286.

Marshall, J., Hill, C., Perelman, L., Adcroft, A., 1997b. Hydrostatic, quasi-hydrostatic, and nonhydrostatic ocean modeling. Journal of Geophysical Research 102, 5733–5752.

Menemenlis, D., Hill, C., Adcroft, A., Campin, J.-M., Cheng, B., Ciotti, B., Fukumori, I., Heimbach, P., Henze, C., Köhl, A., Lee, T., Stammer, D., Taft, J., Zhang, J., 2005. Nasa supercomputer improves prospects for ocean climate research. EOS, Transactions, AGU 86 (9), 89. 95–96.

MITgcm Group, 2002. MITgcm release 1 manual. Technical Report, <http://mitgcm.org/sealion>, Massachusetts Institute of Technology, Cambridge, MA 02139, USA, 346 pp.

Molteni, F., 2003. Atmospheric simulations using a GCM with simplified physical parametrization, I: Model climatology and variability in multidecadal experiments. Climate Dynamics 20, 175–191.

Morales Maqueda, M.A., Biggs, N.R.T., Willmott, A.J., 2004. Polynya dynamics: a review of observations and modeling. Review in Geophysics 42, RG1004.

Prange, M., Gerges, R., 2006. The role of surface freshwater flux boundary conditions in arctic ocean modelling. Ocean Modelling 13, 25–43.

Robert, A., Henderson, J., Turnbull, C., 1972. An implicit time integration scheme for baroclinic models of the atmosphere. Monthly Weather Review 100, 329–335.

Roullet, G., Madec, G., 2000. Salt conservation, free surface, and varying levels: a new formulation for ocean general circulation models. Journal of Geophysical Research 105, 23927–23942.

Russell, G.L., Miller, J.R., Rind, D., 1995. A coupled atmosphere-ocean model for transient climate change. Atmosphere-Ocean 33 (4), 683–730.

Schmidt, G., Bitz, C., Mikolajewicz, U., Tremblay, B., 2004. Ice-ocean boundary conditions for coupled models. Ocean Modelling 7, 59–74.

Stommel, H., 1984. The delicate interplay between wind-stress and buoyancy input in ocean circulation: the goldsbrough variations. Tellus 36A, 111–119.

Tartinville, B., Campin, J.-M., Fichefet, T., Goosse, H., 2001. Realistic representation of the surface freshwater flux in an ice-ocean general circulation model. Ocean Modelling 3, 95–108.

Timmermann, R., Beckmann, A., Hellmer, H.H., 2002. Simulations of ice-ocean dynamics in the Weddell Sea 1. Model configuration and validation. Journal of Geophysical Research 107 (C3), 3024.

Winton, M., 2000. A reformulated three-layer sea ice model. Journal of Atmospheric and Oceanic Technology 17, 525–531.

Zhang, J., Hibler, W.D., 1997. On an efficient numerical method for modeling sea ice dynamics. Journal of Geophysical Research 102, 8691–8702.

Zhang, J., Hibler, W.D., Steele, M., Rothrock, D., 1998. Arctic ice-ocean modeling with and without climate restoring. Journal of Physical Oceanography 28, 191–217.